Am J Cancer Res 2022;12(1):210-228
www.ajcr.us /ISSN:2156-6976/ajcr0138549

Original Article

Photodynamic therapy of melanoma with new, structurally similar, NIR-absorbing ruthenium (II) complexes promotes tumor growth control via distinct hallmarks of immunogenic cell death

Prathyusha Konda[1*], John A Roque III[2,3*], Liubov M Lifshits[2*], Angelita Alcos[4], Eissa Azzam[1], Ge Shi[2], Colin G Cameron[2], Sherri A McFarland[2], Shashi Gujar[1,4,5,6]

[1]Department of Microbiology & Immunology, Dalhousie University, Halifax, Nova Scotia B3H 1X5, Canada; [2]Department of Chemistry and Biochemistry, The University of Texas at Arlington, Arlington, Texas 76019-0065, USA; [3]Department of Chemistry and Biochemistry, The University of North Carolina at Greensboro, Greensboro, North Carolina 27402, USA; [4]Department of Pathology, Dalhousie University, Halifax, Nova Scotia B3H 1X5, Canada; [5]Department of Biology, Dalhousie University, Halifax, Nova Scotia B3H 1X5, Canada; [6]Beatrice Hunter Cancer Research Institute, Halifax, Nova Scotia B3H 1X5, Canada. [*]Equal contributors.

Received August 24, 2021; Accepted October 6, 2021; Epub January 15, 2022; Published January 30, 2022

Abstract: Cancer therapies that generate T cell-based anti-cancer immune responses are critical for clinical success and are favored over traditional therapies. One way to elicit T cell immune responses and generate long-lasting anti-cancer immunity is through induction of immunogenic cell death (ICD), a form of regulated cell death that promotes antigenicity and adjuvanticity within dying cells. Therefore, research in the last decade has focused on developing cancer therapies which stimulate ICD. Herein, we report novel photodynamic therapy (PDT) compounds with immunomodulatory and ICD inducing properties. PDT is a clinically approved, minimally invasive anti-cancer treatment option and has been extensively investigated for its tumor-destroying properties, lower side effects, and immune activation capabilities. In this study, we explore two structurally related ruthenium compounds, ML19B01 and ML19B02, that can be activated with near infrared light to elicit superior cytotoxic properties. In addition to its direct cell killing abilities, we investigated the effect of our PSs on immunological pathways upon activation. PDT treatment with ML19B01 and ML19B02 induced differential expression of reactive oxygen species, proinflammatory response-mediating genes, and heat shock proteins. Dying melanoma cells induced by ML19B01-PDT and ML19B02-PDT contained ICD hallmarks such as calreticulin, ATP, and HMGB1, initiated activation of antigen presenting cells, and were efficiently phagocytosed by bone marrow-derived dendritic cells. Most importantly, despite the distinct profiles of ICD hallmark inducing capacities, vaccination with both PDT-induced dying cancer cells established anti-tumor immunity that protected mice against subsequent challenge with melanoma cells.

Keywords: Immunogenic cell death, cancer immunotherapies, T cells, dendritic cells, photodynamic therapy, melanoma

Introduction

Cancer immunotherapies hold tremendous promise in clinics due to their ability to harness the patient's own immune system to attack tumor cells [1]. Several immunotherapies have been developed by targeting different phases of the cancer-immunity cycle, such as immune checkpoint inhibitors, adoptive T cell transfer therapies, and cancer vaccines [2-5]. T cell-based immunotherapies have become a central focus for generating durable anti-cancer immune responses, due to their capacity for recognizing and eradicating malignant cells through cancer-specific antigen-directed cytotoxicity [5]. Furthermore, T cell infiltration in the tumor microenvironment (TME) has been correlated with control of tumor progression and is deemed a critical factor in the efficacy of immunotherapies [5-8]. Professional antigen presenting cells (APCs) such as dendritic cells (DCs) play a crucial role in the initiation of these

T cell-based immune responses by presenting tumor antigens to T cells thereby activating them [9]. Consequently, therapeutic interventions that promote the DC-T cell-based anti-cancer immunity are highly desired.

In this context, immunogenic cell death (ICD) has garnered attention in recent times, as this form of regulated cell death can activate DCs, induce anti-tumor T cell responses, and generate beneficial long-lasting immunity [10-12]. ICD encompasses diverse 'hallmarks' that ultimately involve two major aspects of anti-tumor T cell response: antigenicity and adjuvanticity. Dying cells undergoing ICD provide access to cancer antigens, which contributes to the antigenicity aspect of ICD [13, 14]. In addition, danger-associated molecular patterns (DAMPs) are emitted spatiotemporally and function as adjuvants in ICD mediated anti-tumor immunity. These DAMPs promote the recruitment and activation of APCs such as DCs by binding to specific pattern recognition receptors (PRRs) on their surface [9, 15, 16]. Activated DCs engulf dying cancer cells, process cancer antigens, and participate in cross-presentation of antigenic peptides to CD8+ T cells, hence activating them and initiating the anti-tumor immune response [9, 17-20]. Numerous preclinical and clinical studies suggest the prognostic and predictive value for DAMPs and associated processes in cancer treatment prognosis [21]. Together, ICD facilitates overturning the TME by recruiting immune cells to the tumor site and converting "cold" tumors to "hot". Therefore, the development of next generation anti-cancer modalities with ICD-inducing properties can improve the clinical outcomes for cancers. Recent efforts have focused on evaluating previously approved chemotherapeutics and developing new agents and therapies for ICD-inducing capabilities [22].

Photodynamic therapy (PDT) is a clinically approved anti-cancer modality that can be used alone or as an adjuvant delivered alongside surgery or other therapies [23]. PDT employs a light-responsive prodrug, known as a photosensitizer (PS), to sensitize cytotoxic reactive oxygen species (ROS) that directly destroy tumors and tumor vasculature [24-28]. The PDT reaction is confined to regions where the PS, light, and oxygen overlap in space and time, thus providing tumor selectivity and fewer side effects compared to conventional therapies. Besides its cytotoxic properties, studies have shown that PDT-induced oxidative stress effectively initiates an inflammatory response and causes the infiltration of immune cells at the treatment site [26, 29, 30]. The acute inflammatory response from PDT is also implicated in the development of adaptive anti-tumor immune responses [31-33]. Recently, PDT has been investigated for its ability to produce ICD and anti-tumor immune responses [34-36], and approaches to improve ICD-inducing capabilities of PDT are being developed [37, 38]. Here, we report the discovery of new ICD-inducing, near infrared (NIR) absorbing ruthenium-based PSs as PDT agents for targeting aggressive melanoma [39, 40].

ML19B01 and ML19B02 are tris heteroleptic Ru(II) complexes containing a chromophoric ligand to shift the absorption into the NIR and a PDT ligand for sensitizing singlet oxygen. Activation of the PS in the NIR window is advantageous for deeper tissue penetration and thus treating a wider tumor margin and may be especially important for highly pigmented melanomas where melanin can effectively compete for light absorption of the shorter wavelengths. PDT generally employs red light and designing new PSs that can be activated with longer wavelength NIR light while maintaining potent photocytotoxic effects has been a major challenge to the field of PS design for PDT. Herein, we not only overcome this hurdle but also demonstrate that both PSs have similar cytotoxic potential but differ in their ICD hallmark-promoting capacities. Additionally, both PDT treatments emit DAMPs in vitro and are efficiently phagocytosed by bone marrow-derived dendritic cells (BMDCs). Using dying cancer cells as tumor vaccination modalities, we demonstrate that the PSs lead to a delay in tumor growth and improve tumor-free survival in the highly aggressive B16F10 mouse melanoma model.

Materials and methods

Spectroscopy

UV-visible-NIR: Electronic absorption spectra were measured on a Jasco v730 spectrometer using dilute (<25 μM) solutions of the complexes in spectroscopy grade acetonitrile in 5 mm

pathlength quartz cuvettes at room temperature. The molar extinction coefficients (ε) were determined by the regression fit of absorption vs concentration for five concentrations.

Ru(II) compound solutions

Stock solutions of metal compounds were prepared at 5 mM in 10% v/v DMSO: water (type 1, ≥ 18.2 MΩ·cm). Stock solutions were stored in glass vials with PTFE-lined caps, protected from light with aluminum foil, and stored at −20°C when not in use. Cellular assays involved ≤ 0.6% v/v DMSO at the highest compound concentration.

Cell culture and PDT treatments

Mouse melanoma cell line B16F10 (ATCC, CRL-6475) was maintained in DMEM cell culture media (Gibco, 11965118) and supplemented with 10% v/v fetal bovine serum (FBS, Gibco, 26140079), 1 mM sodium pyruvate (Gibco, 11360070), 1% v/v non-essential amino acids (Gibco, 11140050), and 1 × antibiotic-antimycotic (Gibco, 15240096). Cells were incubated at 37°C in a humidified atmosphere containing 5% CO_2 and used within 15 passages for all experiments. For all experiments, briefly, B16-F10 cells are seeded into plates and let incubate for 3 h in the incubator before the addition of the photosensitizers at respective concentrations. These plates are then covered in aluminum foil to protect from light and are incubated at 37°C, 5% CO_2 for 16 h upon which PDT treatment plates are exposed to a 630 nm light (Prizmatix LED, UHP-T-LED-630) or 730 nm ((2 W, CivilLaser; (9-10 Mw-2) coupled to a 600 μm optical fiber with a 2 mm flat-cut diffuser (Medlight, FD1)) to achieve required light dosage.

Cytotoxicity assays

Alamar blue cell viability assays were performed according to the protocol previously published [41]. Briefly, 2.5 × 10^4 B16F10 cells were plated in 96-well plates and treated with PSs in the ranges of 0 to 10 μM. PBS was used as a control. After 16 h incubation in the dark, plates were exposed to 100 J cm^{-2} of 630 nm or 730 nm irradiation. Freshly prepared resazurin sodium salt (Sigma, R7017) was added to the plates 48 h post-PDT treatment, and plates were left in the dark for 3 h before analysis on a Spectramax M3. Flow cytometry-based cell death was assessed by Annexin V (Biolegend, 640905) and 7AAD (eBioscience, 00-6993) staining. A total of 2.5 × 10^5 cells were plated in 12-well plates and treated with the determined EC_{50} of compounds and 25 J cm^{-2} of 630 nm irradiation. Briefly, cells were collected 4 h post-treatment, washed, and resuspended in an incubation buffer (10 mM HEPES/NaOH (pH 7.4), 140 mM NaCl, and 5 mM $CaCl_2$) at a total cell concentration of 0.5-1 × 10^6 cells mL^{-1}. Annexin V (5 μL) followed by 7AAD (5 μL) was added to the cell suspension, samples were incubated in the dark for 15 min at room temperature and live samples were acquired on a BD FACS Canto II or BD FACS Celesta flow cytometer.

Flow cytometry assays for surface calreticulin and intracellular ROS analysis

A total of 2.5 × 10^5 cells were plated in 12-well plates and treated with the determined EC_{50} of compounds and 25 J cm^{-2} of 630 nm irradiation. For calreticulin staining, cells were collected by gentle trypsinization 4 h post-treatment, washed twice in cold PBS, incubated for 45 min with the rabbit anti-calreticulin primary antibody (Abcam, ab2907), diluted in cold blocking buffer (1% FBS in PBS), followed by washing and incubation with the Alexa Fluor 647-conjugated secondary antibody (Invitrogen, A-21246) in a blocking buffer for 30 min. Cells were again washed twice with PBS and fixed in 2% paraformaldehyde in PBS for 15 min. For intracellular ROS analysis, trypsinized and washed cells were incubated with CM-H2DCFDA (Molecular Probes, C6827, 1 μM) or MitoSOX (Molecular Probes, M36008) for 30 min at 37°C in PBS before live cell analysis. In both experiments, samples were analyzed on the BD FACS Canto II or BD FACS Celesta to identify cell surface calreticulin.

Detection of ATP secretion and HMGB1 release

A total of 2.5 × 10^5 cells were plated in 12-well plates and treated with the determined EC_{50} of compounds and 25 J cm^{-2} of 630 nm irradiation. Supernatants were collected 12 h post-treatment and their ATP concentrations were measured through an ATP Determination Kit (Invitrogen, A22066), according to the manufacturer's protocol. Similarly, supernatants

Table 1. qRT-PCR primer sequences

Gene name	Forward primer	Reverse primer
CXCL10	GTTGAGATCATTGCCACGATGAAA	CTGCTGTCCATCCATCGCA
IFNβ	GTCCGAGCAGAGATCTTCAGG	GAGTCCGCCTCTGATGCTTA
HSP90	CTCCAATTCATCGGACGCTCT	AAGTCGGCCTTGGTCATTCC
HSP70	CAGGACCCACCATCGAGGA	ACAGTAATCGGTGCCCAAGC
TLR3	TCCTGCTGGAAAACTGGATGG	AGCCTGAAAGTGAAACTCGCT
β2M	ATGCTATCCAGAAAACCCCTCA	TTTCAATGTGAGGCGGGTGG
IL6	TCTCTGCAAGAGACTTCCATCC	TTGTGAAGTAGGGAAGGCCG
IFIT1	ACCATGGGAGAGAATGCTGATG	TTGTGCATCCCCAATGGGTT
TNFα	TGTTGCCTCCTCTTTTGCTT	TGGTCACCAAATCAGCGTTA
TAP1	CCACGAGTGTCTCGGGAAT	ATGAGACAAGGTTGCCGCT
H2D	GAGTGAGCCTGAGGAACCTG	AGCCAGACATCTGCTGGAGT
GAPDH	TGGCAAAGTGGAGATTGTTG	AAGATGGTGATGGGCTTCCC
CD40	TGTCATCTGTGAAAAGGTGGTC	ACTGGAGCAGCGGTGTTATG
CD80	GCAGGATACACCACTCCTCAA	AAAGACGAATCAGCAGCACAA
CD83	CGCAGCTCTCCTATGCAGTG	GTGTTTTGGATCGTCAGGGAATA
CD86	TGTTTCCGTGGAGACGCAAG	TTGAGCCTTTGTAAATGGGCA
CTLA4	AGAACCATGCCCGGATTCTG	CATCTTGCTCAAAGAAACAGCAG
IcosL	TAAAGTGTCCCTGTTTTGTGTCC	ATTGCACCGACTTCAGTCTCT
IL12β	TGGTTTGCCATCGTTTTGCTG	ACAGGTGAGGTTCACTGTTTCT
Arg1	CTCCAAGCCAAAGTCCTTAGAG	AGGAGCTGTCATTAGGGACATC
PD-L1	CCTCGCCTGCAGATAGTTCC	AGCCGTGATAGTAAACGCCC
Tim3	TCAGGTCTTACCCTCAACTGTG	GGCATTCTTACCAACCTCAAACA

were collected 24 h post-treatment and immediately assessed for HMGB1 levels by enzyme-linked immunosorbent assay according to the manufacturer's instructions (IBL International, ST51011). Readings in both cases were taken on a SpectraMax M3 well plate reader.

Real-time qPCR characterization of PDT-treated B16F10 cells

A total of 5×10^5 B16F10 cells were plated in 6-well plates and treated with the determined EC_{50} of compounds and 25 J cm^{-2} of 630 nm irradiation. Cells were collected 12 h post-treatment in TRIzol (Thermo, 15596026) for RNA extraction. RNA extractions were conducted using standard TRIzol methodology as per manufacturer guidelines (Invitrogen, 155960-26 & 12183025). Extracted RNA was quantified, diluted to a total of 2 µg, and synthesized into cDNA using SuperScript II Reverse Transcriptase (Invitrogen, 18064014). The Bio-Rad CFX96 PCR machine was used for qPCR, using Ssoadvanced universal SYBR green supermix (Bio-Rad, 1725274) according to the manufacturer's instructions for amplification and quantification. Gene-specific primers (**Table 1**) for murine HSP90, HSPA1B, CXCL10, TNFα, IL6, IFNβ, IFIT1, TLR3, H2D, TAP1, β2M, CD40, CD80, CD83, CD86, IL12β, IcosL, PD-L1, TIM3, Arg1, CTLA4, and GAPDH were synthesized and purchased from Invitrogen. The data from the qPCR were collected and analyzed using Livak and Schmittgen's 2-ΔΔCT method. The fold change was calculated by first normalizing the cycle threshold (ct) of the indicated gene against GAPDH, followed by comparison against the control untreated sample.

Mice

Wildtype C57BL/6 mice obtained from Charles River (strain code: 027) were utilized for experimental purposes. All in vivo as well as ex vivo experiments used 8-12-week-old mice, housed at Dalhousie University Animal Care Facility. Animal protocols are approved by the Dalhousie University Committee on Laboratory Animals (UCLA; protocol number 18-151).

Generation of bone marrow-derived dendritic cells

Generation of BMDCs followed a stepwise protocol previously described [42]. In short, flushed bone marrow cells collected from mouse femur and tibia were treated with red blood cell-lysing ammonium-chloride-potassium (ACK) buffer (150 mM NH_4Cl, 10 mM $KHCO_3$, 0.1 mM Na_2EDTA). In total, 3×10^6 bone marrow cells were cultured per well in a 6-well plate in RPMI 1640 (Invitrogen, 11875135) supplemented with 10% v/v FBS, 1% v/v Glutamax (Invitrogen, 35050061), 1 mM sodium pyruvate, 1% v/v non-essential amino acids, 1 × antibiotic-antimycotic and 20 ng ml^{-1} growth factor GM-CSF (Biolegend, 576302). On day 3 and day 6, fully supplemented media was added to cultures. Experiments were performed with suspension cells from day 7 to day 9 post differentiation.

BMDC phagocytosis and functional characterization experiments

For phagocytosis experiments, CFSE (Biolegend, 423801) labelled B16F10 cells were treated with determined EC_{50} of compounds and 25 J cm^{-2} of 630 nm irradiation. Cells were collected 4 h post-PDT and co-cultured with harvested BMDCs at 1:1 or 1:5 ratio, for 2 h at 37°C. After co-culture, cells were washed and incubated with anti-mouse CD16/CD32 (BioXCell, BE0307) for 30 min followed by labelling with CD11c-APC/Cy7 (Biolegend, 117323) for 30 min. Cells were acquired on BD FACS Canto II or BD FACS Celesta. For functional characterization, harvested BMDCs were cultured in PDT-treated B16F10 conditioned media (50% of total volume and 50% base DC media as described above) for 24 h at 37°C. LPS treated sample was used as a positive control. Cells were collected in TRIzol (Thermo, 15596026) post-activation with appropriate conditioned medium treatment for qRT-PCR analysis.

Confirmation of ICD with gold-standard in vivo vaccination experiment

A total of 5×10^5 B16F10 cells per well in a 6-well plate were treated with the determined EC_{50} of compounds and 50 J cm^{-2} of 630 nm irradiation. For the vaccination, 4 and 12 h post-treatment cells were combined, and 5×10^5 cells in 100 µL PBS were injected subcutaneously into the left flank of male and female C57BL/6 mice. A week after vaccination, mice were challenged with 1×10^5 untreated B16F10 cells in 100 ul PBS into the right flank. Tumor sizes were measured using a digital vernier caliper and volumes were calculated using formula pi × (length × width × height)/3. Data is collected from 15 animals per group in all groups, except for the group for unvaccinated males which consisted of 13 animals.

Data analysis

Flow cytometry data were analyzed using FCS Express 6 software. Mean fluorescence intensity values (MFI) were reported after subtracting the background fluorescence of respective treatments. qRT-PCR analysis was done using Bio-Rad CFX Manager software. All statistical analyses were performed in GraphPad Prism 7. Hazard ratios were calculated with the Mantel-Haenszel method using GraphPad Prism 7. The hazard ratios represent the hazard rate of the unvaccinated group over the vaccinated group. One-way ANOVA coupled with Bonferroni post-test or Student's t-test was performed and significance is listed as follows: *=P<0.05, **=P<0.01, ***=P<0.001, ****=P<0.0001. All experiments represent data from a minimum of n=3 experiments.

Results

Synthesis and characterization of ruthenium compounds

Ruthenium compound ML18H01 was reported previously [39]. Compounds ML19B01 and ML19B02 were synthesized in 63% and 47% yields, respectively, following a synthetic protocol that we recently described for the synthesis of analogous Ru(II) complexes [39]. Briefly, intermediate [Ru(tpbn)(dppn)(Cl)]Cl [39] was treated with an excess of monodentate pyridine ligand (4-phenylpyridine or 4-dimethylaminopyridine) and subjected to microwave irradiation while heating at 140-150°C. Compounds ML19B01 and ML19B02 were purified using flash column chromatography on alumina and size-exclusion chromatography on Sephadex® LH-20. After purification, the molecular structures of isolated compounds were confirmed with 1D and 2D ^{1}H NMR and high-resolution mass spectrometry, and their purities were confirmed by HPLC analysis.

NMR assignments: The assignments of the ^{1}H NMR signals of Ru(II) complexes ML19B01 and ML19B02 were made based on correlations observed by ^{1}H-^{1}H COSY NMR, based on the values of observed *J*-values, and based on our previously reported assignments of related complexes. Hydrogens from the tpbn ligand (3, 3′, 4′, 5′, 6′, 7′, and 4-tBu) and hydrogens from the dppn ligand (a, b, c, d, e, f, g, h, i, j, k, l) were assigned as we previously described for analogous Ru(II) complexes [39]. Hydrogens from the monodentate pyridine ligands (4-phenylpyridine and 4-dimethylaminopyridine) were assigned similarly as we previously described for the hydrogens of 4-picoline ligand [39]. In the monodentate pyridine ligands, the signal for hydrogen 2″ was the most downfield shifted due to its *ortho*-position relative to the nitrogen. In ML19B01, the next most downfield signal appeared as a doublet of doublets and was assigned to hydrogen 6″ due to the best fit for

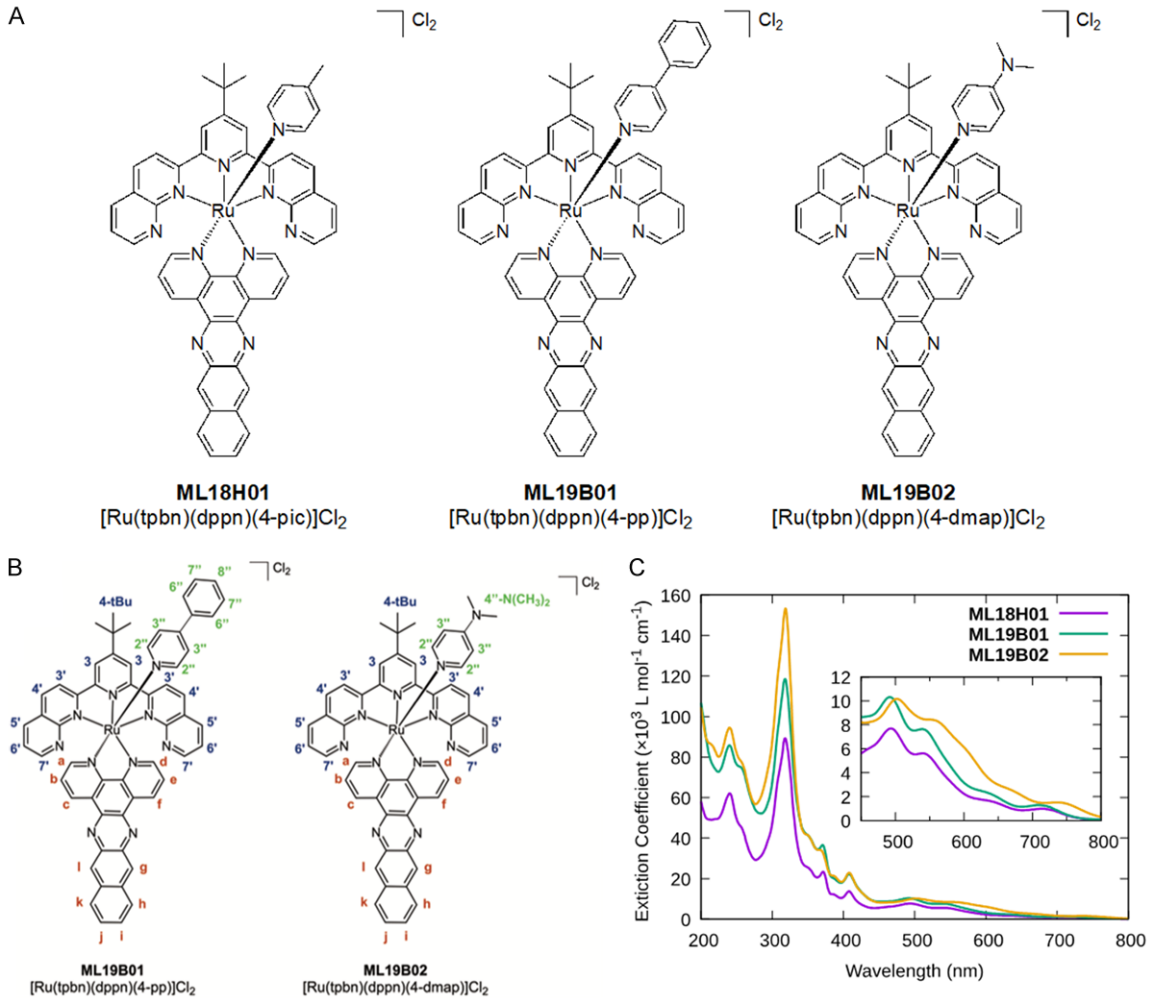

Figure 1. Structures and spectral profiles of the compounds investigated in this study. A. Molecular structures of the two NIR-absorbing and PDT-active ruthenium compounds of this study and the parent complex ML18H01. B. Hydrogen labeling for the purpose of assigning the one and two-dimensional NMR spectra. C. UV-Vis-NIR absorption spectra of the NIR-absorbing and PDT-active ruthenium compounds.

Table 2. Absorption peak maxima (nm) and corresponding molar extinction coefficients (log ε)

COMPOUND	λ_{abs}/nm ($\log_{10}(\varepsilon/M^{-1}\ cm^{-1})$)
ML18H01	240 (4.79), 318 (4.95), 371 (4.37), 408 (4.14), 494 (3.89), 540 (3.75), 634 (3.22), 716 (2.99)
ML19B01	240 (4.93), 318 (5.08), 371 (4.56), 408 (4.34), 492 (4.01), 542 (3.88), 639 (3.33), 710 (3.07)
ML19B02	240 (4.98), 319 (5.19), 408 (4.37), 502 (4.01), 558 (3.93), 671 (3.41), 736 (3.20)

this multiplicity. Hydrogen 3″ is expected to be a clear doublet with a *J*-value matching the *J*-value of a doublet corresponding to 2″, hydrogen 7″ is expected to be a doublet of doublets with two close *J*-values, and hydrogen 8″ is expected to be a triplet of doublets with a small J_2-value, but these three signals (3″, 7″, and 8″) fully overlapped so fine splitting was obscured. In ML19B02, hydrogen 3″ was assigned based on its ^{1}H–^{1}H correlation to 2″.

The electronic absorption spectra of the compounds are shown in **Figure 1**, and the local absorption maxima and extinction coefficients at those peak maxima are tabulated in **Table 2**. The shorter wavelength, sharper peaks (<425 nm) can be ascribed to ππ* ^{1}IL transitions on the ligands and vary in intensity. The dominant peak at approximately 318 nm is diagnostic of the tpbn ligand. Weaker absorptions in the longer wavelength region occur near 540,

635, and 720 nm, corresponding to ^{1}MLCT transitions. The longest wavelength absorption is assigned as the spin-allowed singlet Ru(dπ)→tpbn(π*) transition, in accordance with our earlier findings [39], and is unusually long for a Ru(II) polypyridyl-type complex [43]. The three MLCT peaks observed for ML19B02, having the dimethylaminopyridine monodentate ligand, are bathochromically shifted by around 0.07, 0.10, and 0.05 eV, respectively, compared to the other two complexes. This is consistent with a higher Ru(dπ) energy due to the increased electron density on the metal by this electron-donating monodentate ligand. The result is a red shift of the longest wavelength ^{1}MLCT absorption bands. We have observed this shift in NIR absorption energy previously for analogous chloro complexes. The data indicate that the two new photosensitizers, like ML18H01, are panchromatic light absorbers from the ultraviolet to the visible region as well as the NIR. The [Ru(tpbn)(dppn)(L)]Cl_2 construct is a robust scaffold for generating NIR absorption well past 700 nm and extending all the way out to 800 nm. Further, the scaffold not only tolerates changes to the monodentate ligand L without compromising its NIR absorption but can be fine-tuned by minor substituent changes to this ligand in order to improve its NIR absorption characteristics.

ML19B01-PDT and ML19B02-PDT induce cell death in melanoma cells

Next, to understand the anti-cancer potential of ML19B01 and ML19B02 PSs, we first analyzed their capacity to induce cell death in B16F10 mouse melanoma cells upon activation with 630 nm red light or 730 nm NIR light. The shorter wavelength was selected because it is the wavelength used for clinically approved Photofrin-PDT, and 730 nm was used as the NIR wavelength because it is the longest wavelength that produced a PDT effect for our previously reported ML18H01 [39]. Briefly, B16F10 cells were treated with increasing concentrations of the PS, incubated in the dark for 16 h, and then irradiated for a total fluence of 100 J cm^{-2} at an irradiance of 22.8 mW cm^{-2} (**Figure 2A**). An analogous set of controls were included that were treated in the same manner; except they did not receive a light treatment but instead were incubated in the dark throughout the experiment. The alamar blue cell viability assay revealed that ML19B01 and ML19B02 did not induce cell death in concentrations of up to 50 μM in dark conditions. Irradiation of PS-treated cells with 630 nm red light resulted in cell death (**Figure 2B**) wherein ML19B01- and ML19B02-PDT had EC_{50} values of 1.14 μM and 2.19 μM, respectively. ML19B01 and ML19B02 showed a similar EC_{50} profile (1.59 μM and 2.51 μM, respectively) with 730 nm NIR light, confirming activation and cell death at both wavelengths. Further analysis was performed with 630 nm as the clinically approved wavelength for PDT with Photofrin. Cell death analysis with Annexin V/7AAD flow cytometry using cells treated with ML19B01 and ML19B02 at their respective EC_{50} values and irradiated with a fluence of 25 J cm^{-2} revealed similar cell death characteristics for both the PSs, as represented by percentages of pre-apoptotic and apoptotic cell populations (**Figure 2D**). The data confirmed that no cell death occurred in the absence of the light treatment. Therefore, the red EC_{50} values were used for subsequent immunological analysis for both the PSs.

ML19B01-PDT and ML19B02-PDT produce distinct immunomodulatory responses

Recent studies have revealed the potential for PDT-induced oxidative stress to result in an inflammatory response [29]. We previously designed one such Ru(II) PS, ML18H01, which efficiently induced multiple proinflammatory pathways that can overturn the immunosuppressive TME in most cancers [39]. To this end, we examined the immunomodulatory effects of ML19B01- and ML19B02-PDT in B16F10 melanoma cells. Treatment of B16F10 cells with ML19B01 and ML19B02 at their respective EC_{50} values, followed by irradiation (630 nm, 25 J cm^{-2}, 22.8 mW cm^{-2}) resulted in differential modulation of immunological pathways. ML19B01-PDT resulted in superior induction of heat shock proteins (HSPs), HSP70, and HSP90 whereas ML19B02 did not result in a significant induction (**Figure 3B**). While both the PSs resulted in induction of proinflammatory cytokines CXCL10 [13], IL6 [13, 44], TNFα [13], and the type 1 interferon (T1 IFN) pathway [13, 45] associated gene IFIT1, the magnitude of expression was higher upon ML19B02-PDT as compared to ML19B01-PDT (**Figure 3C**, **3D**). Neither PS altered the expression of other

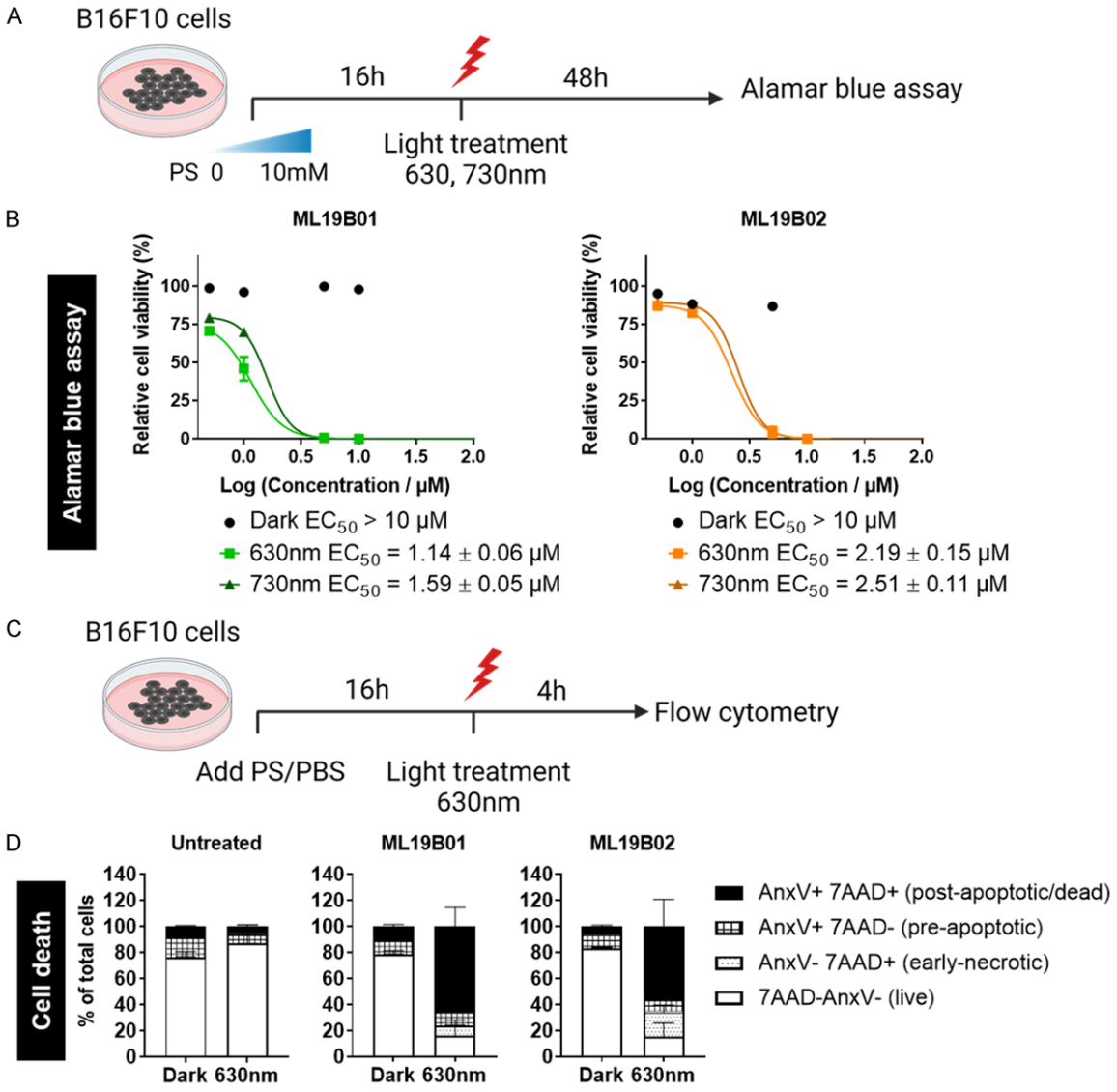

Figure 2. Cell death analysis in B16F10 cells treated with ML19B01-PDT or ML19B02-PDT. A. Schematic representation of alamar blue cell viability assay. B. Cell viability graphs indicating respective EC_{50} values for different conditions. Treatments include both PSs or PBS with and without light treatment (630 nm and 730 nm). C. Schematic representation of the experimental strategy for cell death analysis via flow cytometry. D. Bar plots indicating the percentages of cell death in different phases. Percentages of pre-apoptotic (7AAD- Annexin V+), post-apoptotic (7AAD+ Annexin V+), early necrotic (7AAD+ Annexin V-) and live (7AAD- Annexin V-) cell populations are plotted.

genes related to the T1 IFN pathway, (IFNβ, TLR3) or those associated with the MHC-I molecule [46, 47] (H2D, β2M, TAP1). Additionally, ML19B01 and ML19B02 under the dark condition did not affect the expression of any of the genes tested (**Figure 3B**). Together these results demonstrate the differential immunomodulatory capacities of ML19B01- and ML19B02-PDT.

PDT-induced cell death is usually characterized by an oxidative stress response and generation of ROS, both of which are implicated in ICD [11, 13]. Moreover, HSPs function as molecular chaperones in response to ICD induced oxidative stress [11, 34, 48]. Therefore, we studied the generation of ROS with ML19B01- and ML19B02-PDT using B16F10 cells. Treatment with ML19B01-PDT but not ML19B02-PDT resulted in an increase in cellular ROS expression, quantified by flow cytometry staining with DCFDA (**Figure 3E**). Flow cytometry staining with Mitosox revealed an increase in mitochondrial ROS with both PSs, but a higher increase

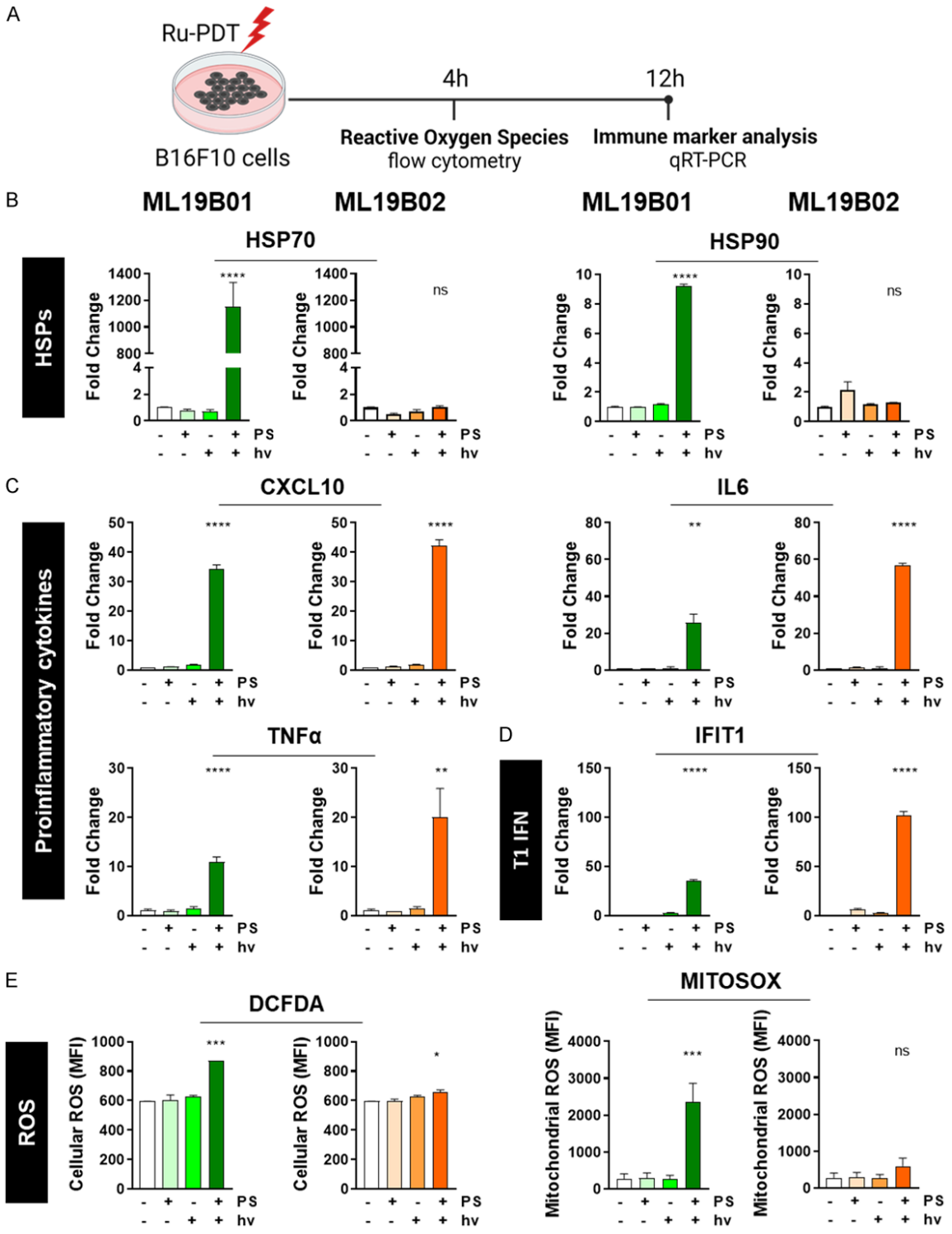

Figure 3. ML19B01 and ML19B02-PDT induce differential modulation of immunological pathways. (A) Schematic representation of the experimental strategy for immune marker analysis and ROS analysis upon PDT treatment. (B-D) qRT-PCR analysis of PDT treated B16F10 cells for genes associated with (B) heat shock proteins, HSP90 and HSP70. (C) Proinflammatory cytokines, CXCL10, IL6, TNFα. (D) Type 1 interferon pathway associated gene IFIT1. Fold changes are relative to untreated samples and normalized to the control gene, GAPDH. (E) Mean fluorescence intensities for ROS, analyzed by flow cytometry for cellular ROS (DCFDA) and mitochondrial ROS (MitoSOX). PS: compound. hv: light treatment.

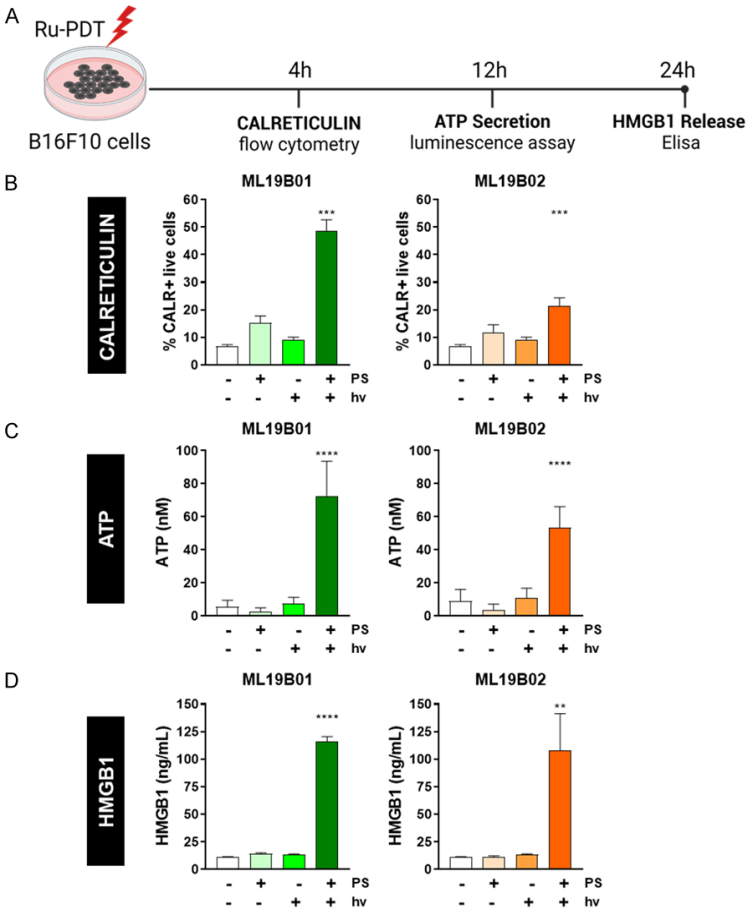

Figure 4. Cell death generated by ML19B01 and ML19B02-PDT induces hallmarks of immunogenic cell death in B16F10 cells. A. Schematic representation of the experimental strategy for analysis of surface calreticulin (CALR) expression, ATP secretion, and HMGB1 release upon PDT treatment of B16F10 cells. B. Flow cytometry analysis of surface expression of CALR in B16F10 cells in vitro. C. Extracellular ATP analysis in B16F10 cells in vitro. D. Analysis of HMGB1 release in supernatant samples of PDT treated B16F10 cells. PS: compound. hv: light treatment.

was observed with ML19B01-PDT compared to ML19B02-PDT (**Figure 3E**). These observations demonstrate the differential regulation of ROS upon treatment with ML19B01- and ML19B02-PDT.

Cell death by ML19B01-PDT and ML19B02-PDT is associated with the emission of DAMPs

ICD has been recognized as one of the promising ways to reverse cancer cell immune evasion and the immunosuppressive TME [49]. Considering the immunomodulatory capacity of ML19B01- and ML19B02-PDT (**Figure 3**) and the roles of HSPs as well as ROS in ICD, we then explored whether the cell death associated with ML19B01- and ML19B02-PDT resulted in the emission of DAMPs. Here, we investigated the major ICD hallmarks [13], calreticulin (CALR) surface translocation [50], ATP secretion [51], and HMGB1 release [52], (which play an important role in anti-tumor immunity due to interactions with the innate immune system) in B16F10 cells treated with ML19B01- and ML19B02-PDT (**Figure 4A**). Surface CALR in ICD stimulates the uptake of dead-cell-associated antigens by DCs, ATP facilitates the recruitment of APCs and their activation, and HMGB1 promotes the activation of DCs and antigen presentation by DCs to T cells [11, 13]. Flow cytometry analysis of B16F10 cells revealed a significant increase of surface CALR expression upon ML19B01-PDT (**Figure 4B**). While ML19B02-PDT resulted in a statistically significant increase in CALR expression, it is much lower compared to ML19B01-PDT. Additionally, ML19B01- and ML19B02-PDT treatment increased the extracellular secretion of ATP (**Figure 4C**) as well as HMGB1 (**Figure 4D**) in the culture supernatants of B16F10 cells. Together, these data revealed the distinct ICD hallmark-inducing capacity of ML19B01- and ML19B02-PDT in mouse melanoma cells in vitro.

ML19B01- and ML19B02-PDT treated cancer cells are phagocytosed by and induce functional markers in BMDCs

DCs, professional antigen presenting cells, play an important role in antigen presentation and priming of CD8+ T cells [9]. As such, successful activation and maturation of DCs have been identified as essential for initiation of the anti-tumor immune responses during ICD [16]. Here, we used GM-CSF differentiated DCs from mouse bone marrow [42] to assess in vitro phagocytosis of B16F10 cells treated with

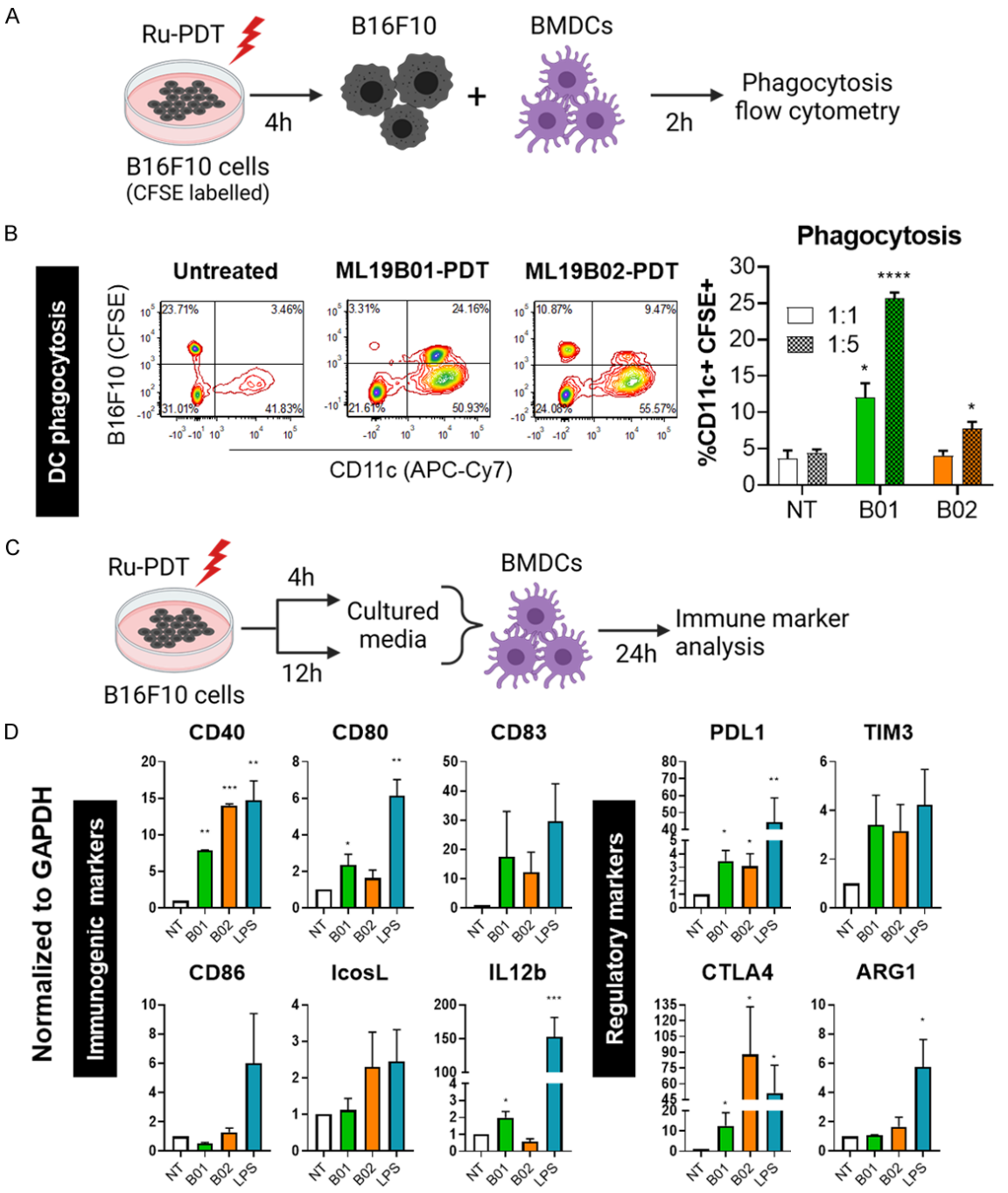

Figure 5. ML19B01 and ML19B02-PDT treated cells are engulfed by BMDCs and induce BMDC functional markers. A. A schematic representation of the workflow for BMDC phagocytosis experiment. B. Contour plots depicting uptake of CFSE labelled B16F10 cells by CD11c+ cells. CD11c+ CFSE+ population in the upper right quadrant indicates the percentage of phagocytosed cells. Representative contour plots represent 1:5 ratio of BMDC: cancer cells. Corresponding bar plot on the right-side depicting percentage CD11c+ CFSE+ cells with 1:1 and 1:5 ratio of BMDC: cancer cells. C. A schematic representation of the experimental strategy for immune marker analysis in DCs upon incubation with PDT-treated conditioned media. D. qRT-PCR analysis of immunogenic markers CD40, CD80, CD83, CD86, IcosL, IL12b and regulatory markers PDL1, TIM3, CTLA4, ARG1. Fold changes are relative to untreated samples and normalized to the control gene, GAPDH. LPS treated sample was used as a positive control.

ML19B01- and ML19B02-PDT (**Figure 5A**). Co-culture of DCs with live vs PDT-treated resulted in phagocytosis of only PDT-treated cells (**Figure 5B**). ML19B01-PDT treated cells

were phagocytosed better than ML19B02-PDT treated B16F10 cells. The rate of phagocytosis also increased with an increase of BMDCs: cancer cell ratio from 1:1 to 1:5. This data shows that dying cancer cells upon PDT-treatment are being phagocytosed by DCs.

Next, we evaluated the immunomodulatory effects of DAMPs released upon PDT-treatment on BMDC maturation, by treating the BMDCs with culture supernatant from ML19B01- or ML19B02-PDT treated B16F10 cells (**Figure 5C**). Analysis of mRNA expression of immunogenic or activation markers of DCs revealed an increase in expression of CD40 [53], CD80 [54, 55], and CD83 [56] upon culture with PDT-treated supernatants. Both ML19B01- and ML19B02-PDT-treated conditioned media increased the expression of these markers but by different magnitudes (**Figure 5D**). In addition to the immunogenic markers, we assessed the expression of several regulatory markers in BMDCs treated with conditioned media from PDT-treated B16F10 cells. Here, we identified an increase in expression of inhibitory PDL1 [57, 58] as well as CTLA4 [59, 60] in BMDCs cultured in ML19B01- and ML19B02-PDT treated B16F10 supernatants. There was no effect on additional immunogenic markers CD86, IL12b, and regulatory markers TIM3 [61] and Arg1 [62]. This data shows that conditioned media from PDT-treated B16F10 cells promotes the expression of immunogenic as well as regulatory markers on DCs.

Collectively, these results indicate that along with the secretion of immunogenic DAMPs, the ML19B01- and ML19B02-PDT-compromised cells are efficiently engulfed by BMDCs, and ML19B01- and ML19B02-PDT increases the expression of DC functional markers.

Vaccination with ML19B01-PDT and ML19B02-PDT-treated cancer cells results in delay of tumor growth and enhanced survival

To evaluate the therapeutic potential of ICD induced by our PSs, we performed the gold standard ICD confirmation experiment [13, 63]. First, mouse B16F10 melanoma cells were treated in vitro at concentrations corresponding to the EC_{50} values of ML19B01- or ML19B02-PDT, and dying cells were collected 4 and 12 h post-treatment and injected into the left flank of C57BL/6 mice for vaccination (**Figure 6A**). These mice were then challenged with untreated B16F10 cells on the right flank 7 days post-vaccination and assessed for tumor growth and tumor-free survival. Mice vaccinated with ML19B01- and ML19B02-PDT treated dying cancer cells displayed improved tumor-free survival and delay in tumor growth compared to unvaccinated control mice (**Figure 6B**). Despite the differential ICD-inducing capacities, the in vivo anti-tumor effects imparted by ML19B01- and ML19B02-PDT were comparable and statistically indistinguishable. This data shows that vaccination with B16F10 cells treated with ML19B01- and ML19B02-PDT produced similar protection against tumor challenge.

The influence of sex differences on cancer incidence, mortality, and treatment outcomes has become increasingly evident in the past decade [64, 65]. To understand the impact of sex on the outcome of ICD-induced anti-tumor protection against melanoma, we performed the vaccination experiment in both female and male mice. Comparison between male and female C57BL/6 mice showed equivalent tumor-free survival. However, vaccinated female mice demonstrated statistically significant superior tumor growth control as compared to vaccinated male mice (**Figure 6C**, **6D**). Together, these results indicate the induction of beneficial anti-tumor protection in C57BL/6 mice upon vaccination with ML19B01 and ML19B02-PDT treated B16F10 cells in a sex-biased manner.

Discussion

In our quest to develop effective immunostimulatory PDT as adjuvant therapy for the most aggressive melanomas, we recently reported Ru-based coordination complexes designed to absorb and be activated with NIR light to achieve potent cytotoxicity in melanoma cells. In our previous study, we used coordination chemistry as a powerful tool to rapidly generate a library of Ru-based PSs with ideal properties for melanoma PDT. Importantly, we established structure-activity relationships to develop the relevant photophysical models for optimizing NIR PDT effects toward melanoma cells and identified several lead Ru(II) PSs. We further explored the immunomodulating properties of PDT with lead ML18H01. The structural scaffold of ML18H01 allows for variation of a monodentate pyridyl-based ligand without compromising the attractive features of NIR absorption

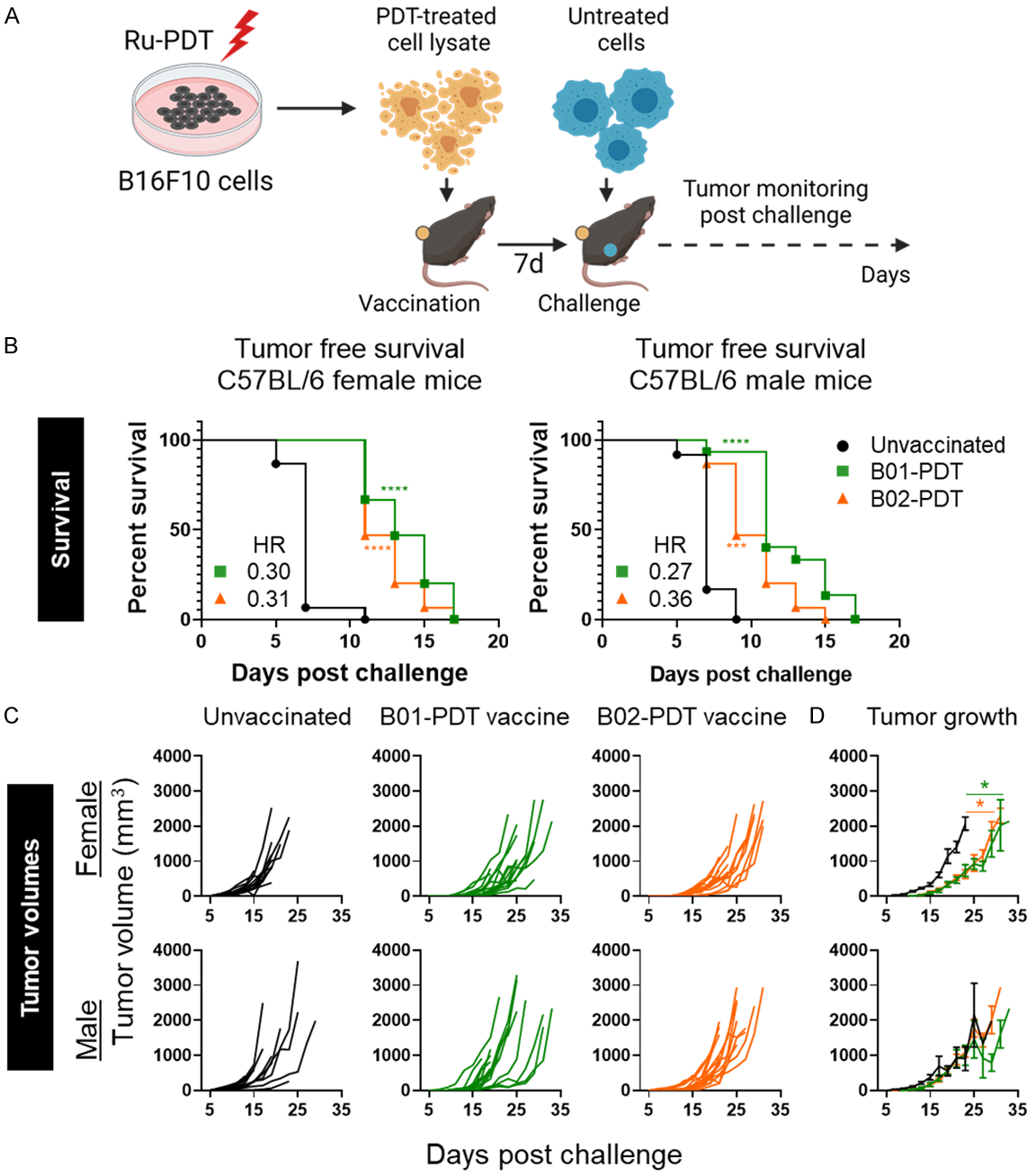

Figure 6. Immunization with ML19B01 and ML19B02-PDT treated cancer cells prolongs tumor-free survival and delays tumor growth in the B16F10 mouse melanoma model. A. Schematic representation of the workflow for the in vivo vaccination experiment. Male and female C57BL/6 mice were first immunized with PDT-treated cells on the left flank, challenged 7 days later with untreated live cells on the right flank, and monitored for tumor growth and survival. B. Tumor-free survival graphs in male and female mice vaccinated with ML19B01 or ML19B02-PDT treated B16F10 cells. Hazard ratio (HR) values are indicated within the graphs. C, D. Tumor growth comparison for unvaccinated vs vaccinated male and female mice, individual groups as well as combined mean tumor growth graphs. Each group represents data from 15 mice, except for the unvaccinated male group, which has 13 mice.

and PDT potency. Modifications at this position provide a convenient handle for fine-tuning biological activity, and our current study with ML19B01 and ML19B02 as next-generation NIR Ru PSs illustrates that the favorable bulk PDT properties are retained while the in vitro immunological signatures can be varied. In the longer term, optimization of these signatures

through structural variation may prove useful for directing anti-tumor responses in vivo, with the goal being to maximize immunoprotective effects in melanoma treatment.

Recent studies, both preclinical and clinical, have demonstrated the ability of PDT to initiate innate and adaptive immune responses against tumors. In this context, ICD of cancer cells is considered a promising way to activate the anti-tumor T cell and DC-based immune responses and achieve ultimate tumor cell clearance. We evaluated the immunological consequences in the context of ML19B01- and ML19B02-PDT-associated cytotoxicity in the B16F10 melanoma model. By analyzing qRT-PCR based gene expression, we found that the two PSs differentially modulate proinflammatory markers and heat shock proteins, both of which play a key role in PDT-associated anti-tumor immunity. While ML19B01-PDT led to a significant increase in HSP90 and HSP70, ML19B02-PDT produced a higher increase in proinflammatory cytokines IL6, TNFα, and CXCL10 compared to ML19B01-PDT. Light treatment alone or PS in the dark condition did not affect the expression of these genes, confirming that the increase only occurred when the PS was activated by light. Interestingly, analysis of ROS revealed that ML19B01-PDT induces higher cellular as well as mitochondrial ROS as compared to ML19B02-PDT. HSPs and ROS are both involved in PDT-mediated oxidative stress, and are also implicated in ICD; here, HSPs act as eat me signals [66], and ROS is involved in the unfolded protein response-mediated exposure of endoplasmic reticulon chaperone CALR to the cell surface [11, 67].

Several hallmarks or signatures of ICD have been discovered in the context of different therapies [13, 49]. For PDT, where ICD is not completely characterized, CALR surface expression, ATP secretion, and HMGB1 release are suggested as core hallmarks. CALR exposure in dying cells is a crucial “eat me” signal during ICD and facilitates the recognition of dying cancer cells by phagocytic cells such as DCs. Along similar lines with HSP and ROS expression, surface translocation of CALR was higher upon ML19B01-PDT treatment than ML19B02-PDT in B16F10 melanoma cells. After CALR exposure, late-stage dying cells secrete ATP and HMGB1 molecules extracellularly, both of which can interact with PRRs on DCs and activate them in vivo. Studies on ATP secretion and HMGB1 release showed a similar increase of both hallmarks with ML19B01- as well as ML19B02-PDT. Together, these findings reveal the immunomodulatory and ICD hallmark-inducing potential for ML19B01- as well as ML19B02-PDT.

Since DAMPs interact with DCs, which play a crucial role in stimulating anti-tumor immune responses, we sought to identify the capacity of PDT-treated dying cancer cells to be phagocytosed. Phagocytosis of cancer cells is a key event which leads to the processing of antigens and eventually, the presentation of antigen by DCs to T cells, therefore impacting the anti-cancer immunity. Both ML19B01 and ML19-B02-PDT treated B16F10 cells were efficiently engulfed by BMDCs in a dose-dependent manner, with ML19B01-PDT treated cells resulting in higher phagocytosis. Because CALR plays an important role in DC phagocytosis [68-70], this data agrees with our observation wherein ML19B01-PDT induced higher surface CALR than ML19B02-PDT. Despite the differences in levels of phagocytosis, culture media from both ML19B01- and ML19B02-PDT treated cells was able to upregulate the expression of immunogenic markers in BMDCs. It is possible that while the ER chaperones HSPs and CALR were differentially regulated by ML19B01- and ML19B02-PDT, leading to a difference in phagocytosis, other DAMPs which were comparable between both groups were able to compensate for the difference in BMDC stimulation. Both ML19B01- and ML19B02-PDT increased the expression of CD40, CD80, and CD83 genes, all associated with activation of BMDCs, but to different extents. Interestingly, we also noted the upregulation of inhibitory genes upon treatment with conditioned media from both compounds. Conditioned media from ML19B01 and ML19B02-PDT treated B16F10 cells increased the expression of PDL1 and CTLA4 genes, both identified as regulatory markers of DC maturation.

While in vitro release of DAMPs provides an indication of ICD, ultimately, their ability to trigger anti-tumor immune responses in vivo is the end goal. To validate the ICD in vivo and furthermore, to understand whether the differences in levels of some ICD hallmarks in vitro translates

to the response in vivo, we performed the gold standard vaccination experiments in immunocompetent C57BL/6 mice [63]. Of note, to understand the possible sex-biased immune responses in the ICD mediated response, we performed this experiment with both male and female C57BL/6 mice. Vaccination of mice with dying B16F10 cancer cells from ML19B01- or ML19B02-PDT treatment resulted in a delay in tumor growth and overall improvement in tumor-free survival as compared to unvaccinated mice, upon challenge with live B16F10 cells. Additionally, both ML19B01-PDT, as well as ML19B02-PDT treated cells provided comparable protection from tumor growth.

Although both male and female mice showed improved tumor-free survival upon vaccination with PDT-treated cells, the control of tumor growth was greater and statistically significant in female mice compared to male mice, indicating a better anti-tumor immune response in female mice. This agrees with our previous findings with ML18H01-PDT, where we found sex-biased differences in the vaccination efficacy of Ru(II) PDT-treated cells in female and male mice. Moreover, preclinical and clinical data in melanoma provides evidence for sex-biased differences in immune responses, tumor development as well as response to therapies, particularly immunotherapies [65, 71-74]. However, neither group was fully protected against tumor growth, and mice vaccinated with either ML19B01- or ML19B02-treated cancer cells eventually formed tumors. There could be two explanations behind this observation. While we noticed efficient induction of immunostimulatory DAMPs, studies have associated the hindrance of ICD with inhibitory DAMPs (iDAMPs), which could play a role in the context of our treatment [68, 75]. A recent study identified prostaglandin E2 as an iDAMP released in response to gemcitabine treatment and blocking this iDAMP reversed the outcome of gemcitabine-induced ICD [76, 77]. Some ICD associated DAMPs are shown to have dual roles, both immunogenic as well as immune-inhibitory or suppressive, depending on their mutations, epigenetic modifications, dose, mode, time of release, and interactions in the TME [75, 78-81]. Additionally, our findings from the in vitro BMDC experiments identified upregulation of inhibitory genes PDL1 and CTLA4 in BMDCs exposed to conditioned media from PDT-treated cells, suggesting that PDT with ML19B01 and ML19B02 triggers the release of these important regulatory molecules. A similar increase of these checkpoint molecules in vivo upon vaccination can result in inefficient stimulation of DC activation, maturation, and T cell activation [57, 82-85]. By exploiting these observations, we hope to design combination therapies with checkpoint inhibitors or by blocking iDAMPs to improve the efficacy of these treatments [86]. However, considering the highly aggressive and poorly immunogenic nature of B16F10 melanoma, the extent of protection observed from our study was notable. Moreover, our study confirms yet again, the importance of performing in vivo vaccination to validate the concept of ICD. Overall, we report two novel ruthenium compounds with cytotoxic as well as immunomodulatory capacities for PDT of metastatic melanoma.

Acknowledgements

S. G. and S. A. M. thank the National Cancer Institute (NCI) of the National Institutes of Health (NIH) (Award R01CA222227) for support. The content in this article is solely the responsibility of the authors and does not necessarily represent the official views of the National Institutes of Health. S. G. notes that the schematic figures were created with https://www.BioRender.com.

Disclosure of conflict of interest

None.

Address correspondence to: Shashi Gujar, Department of Pathology, Dalhousie University, Halifax, Nova Scotia B3H 1X5, Canada. E-mail: shashi.gujar@dal.ca; Sherri A McFarland and Colin G Cameron, Department of Chemistry and Biochemistry, University of Texas at Arlington, Arlington 76019-0065, Texas, USA. E-mail: sherri.mcfarland@uta.edu (SAM); colin.cameron@uta.edu (CGC)

References

[1] Hou J, Karin M and Sun B. Targeting cancer-promoting inflammation - have anti-inflammatory therapies come of age? Nat Rev Clin Oncol 2021; 18: 261-279.

[2] Zhang Y and Zhang Z. The history and advances in cancer immunotherapy: understanding the characteristics of tumor-infiltrating immune cells and their therapeutic implications. Cell Mol Immunol 2020; 17: 807-821.

[3] Hiam-Galvez KJ, Allen BM and Spitzer MH. Systemic immunity in cancer. Nat Rev Cancer 2021; 21: 345-359.
[4] Varadé J, Magadán S and González-Fernández Á. Human immunology and immunotherapy: main achievements and challenges. Cell Mol Immunol 2021; 18: 805-828.
[5] Waldman AD, Fritz JM and Lenardo MJ. A guide to cancer immunotherapy: from T cell basic science to clinical practice. Nat Rev Immunol 2020; 20: 651-668.
[6] Trujillo JA, Sweis RF, Bao R and Luke JJ. T cell-inflamed versus non-T cell-inflamed tumors: a conceptual framework for cancer immunotherapy drug development and combination therapy selection. Cancer Immunol Res 2018; 6: 990-1000.
[7] Zhang J, Endres S and Kobold S. Enhancing tumor T cell infiltration to enable cancer immunotherapy. Immunotherapy 2019; 11: 201-213.
[8] Li X, Gruosso T, Zuo D, Omeroglu A, Meterissian S, Guiot MC, Salazar A, Park M and Levine H. Infiltration of CD8+ T cells into tumor cell clusters in triple-negative breast cancer. Proc Natl Acad Sci U S A 2019; 116: 3678-3687.
[9] Wculek SK, Cueto FJ, Mujal AM, Melero I, Krummel MF and Sancho D. Dendritic cells in cancer immunology and immunotherapy. Nat Rev Immunol 2020; 20: 7-24.
[10] Fucikova J, Kepp O, Kasikova L, Petroni G, Yamazaki T, Liu P, Zhao L, Spisek R, Kroemer G and Galluzzi L. Detection of immunogenic cell death and its relevance for cancer therapy. Cell Death Dis 2020; 11: 1013.
[11] Galluzzi L, Buqué A, Kepp O, Zitvogel L and Kroemer G. Immunogenic cell death in cancer and infectious disease. Nat Rev Immunol 2017; 17: 97-111.
[12] Green DR, Ferguson T, Zitvogel L and Kroemer G. Immunogenic and tolerogenic cell death. Nat Rev Immunol 2009; 9: 353-363.
[13] Galluzzi L, Vitale I, Warren S, Adjemian S, Agostinis P, Martinez AB, Chan TA, Coukos G, Demaria S, Deutsch E, Draganov D, Edelson RL, Formenti SC, Fucikova J, Gabriele L, Gaipl US, Gameiro SR, Garg AD, Golden E, Han J, Harrington KJ, Hemminki A, Hodge JW, Hossain DMS, Illidge T, Karin M, Kaufman HL, Kepp O, Kroemer G, Lasarte JJ, Loi S, Lotze MT, Manic G, Merghoub T, Melcher AA, Mossman KL, Prosper F, Rekdal Ø, Rescigno M, Riganti C, Sistigu A, Smyth MJ, Spisek R, Stagg J, Strauss BE, Tang D, Tatsuno K, van Gool SW, Vandenabeele P, Yamazaki T, Zamarin D, Zitvogel L, Cesano A and Marincola FM. Consensus guidelines for the definition, detection and interpretation of immunogenic cell death. J Immunother Cancer 2020; 8: e000337.
[14] Kepp O, Senovilla L, Vitale I, Vacchelli E, Adjemian S, Agostinis P, Apetoh L, Aranda F, Barnaba V, Bloy N, Bracci L, Breckpot K, Brough D, Buqué A, Castro MG, Cirone M, Colombo MI, Cremer I, Demaria S, Dini L, Eliopoulos AG, Faggioni A, Formenti SC, Fučíková J, Gabriele L, Gaipl US, Galon J, Garg A, Ghiringhelli F, Giese NA, Guo ZS, Hemminki A, Herrmann M, Hodge JW, Holdenrieder S, Honeychurch J, Hu HM, Huang X, Illidge TM, Kono K, Korbelik M, Krysko DV, Loi S, Lowenstein PR, Lugli E, Ma Y, Madeo F, Manfredi AA, Martins I, Mavilio D, Menger L, Merendino N, Michaud M, Mignot G, Mossman KL, Multhoff G, Oehler R, Palombo F, Panaretakis T, Pol J, Proietti E, Ricci JE, Riganti C, Rovere-Querini P, Rubartelli A, Sistigu A, Smyth MJ, Sonnemann J, Spisek R, Stagg J, Sukkurwala AQ, Tartour E, Thorburn A, Thorne SH, Vandenabeele P, Velotti F, Workenhe ST, Yang H, Zong WX, Zitvogel L, Kroemer G and Galluzzi L. Consensus guidelines for the detection of immunogenic cell death. Oncoimmunology 2014; 3: e955691.
[15] Yatim N, Cullen S and Albert ML. Dying cells actively regulate adaptive immune responses. Nat Rev Immunol 2017; 17: 262-275.
[16] Edukulla R, Ramakrishna E, Woller N, Mundt B, Knocke S, Gürlevik E, Saborowski M, Malek N, Manns MP, Wirth T, Kühnel F and Kubicka S. Antitumoral immune response by recruitment and expansion of dendritic cells in tumors infected with telomerase-dependent oncolytic viruses. Cancer Res 2009; 69: 1448-1458.
[17] Embgenbroich M and Burgdorf S. Current concepts of antigen cross-presentation. Front Immunol 2018; 9: 1643.
[18] Galluzzi L, Senovilla L, Vacchelli E, Eggermont A, Fridman WH, Galon J, Sautès-Fridman C, Tartour E, Zitvogel L and Kroemer G. Trial watch: dendritic cell-based interventions for cancer therapy. Oncoimmunology 2012; 1: 1111-1134.
[19] Gu YZ, Zhao X and Song XR. Ex vivo pulsed dendritic cell vaccination against cancer. Acta Pharmacol Sin 2020; 41: 959-969.
[20] Harari A, Graciotti M, Bassani-Sternberg M and Kandalaft LE. Antitumour dendritic cell vaccination in a priming and boosting approach. Nat Rev Drug Discov 2020; 19: 635-652.
[21] Fucikova J, Moserova I, Urbanova L, Bezu L, Kepp O, Cremer I, Salek C, Strnad P, Kroemer G, Galluzzi L and Spisek R. Prognostic and predictive value of DAMPs and DAMP-associated processes in cancer. Front Immunol 2015; 6: 402.
[22] Wang Q, Ju X, Wang J, Fan Y, Ren M and Zhang H. Immunogenic cell death in anticancer chemotherapy and its impact on clinical studies. Cancer Lett 2018; 438: 17-23.

[23] Dougherty TJ, Gomer CJ, Henderson BW, Jori G, Kessel D, Korbelik M, Moan J and Peng Q. Photodynamic therapy. J Natl Cancer Inst 1998; 90: 889-905.
[24] Sharman WM, Allen CM and van Lier JE. Photodynamic therapeutics: basic principles and clinical applications. Drug Discov Today 1999; 4: 507-517.
[25] Plaetzer K, Krammer B, Berlanda J, Berr F and Kiesslich T. Photophysics and photochemistry of photodynamic therapy: fundamental aspects. Lasers Med Sci 2009; 24: 259-268.
[26] Agostinis P, Berg K, Cengel KA, Foster TH, Girotti AW, Gollnick SO, Hahn SM, Hamblin MR, Juzeniene A, Kessel D, Korbelik M, Moan J, Mroz P, Nowis D, Piette J, Wilson BC and Golab J. Photodynamic therapy of cancer: an update. CA Cancer J Clin 2011; 61: 250-281.
[27] Benov L. Photodynamic therapy: current status and future directions. Med Princ Pract 2015; 24 Suppl 1: 14-28.
[28] van Straten D, Mashayekhi V, de Bruijn HS, Oliveira S and Robinson DJ. Oncologic photodynamic therapy: basic principles, current clinical status and future directions. Cancers 2017; 9: E19.
[29] Donohoe C, Senge MO, Arnaut LG and Gomes-da-Silva LC. Cell death in photodynamic therapy: from oxidative stress to anti-tumor immunity. Biochim Biophys Acta Rev Cancer 2019; 1872: 188308.
[30] Falk-Mahapatra R and Gollnick SO. Photodynamic therapy and immunity: an update. Photochem Photobiol 2020; 96: 550-559.
[31] Beltrán Hernández I, Yu Y, Ossendorp F, Korbelik M and Oliveira S. Preclinical and clinical evidence of immune responses triggered in oncologic photodynamic therapy: clinical recommendations. J Clin Med 2020; 9: E333.
[32] Gollnick SO and Brackett CM. Enhancement of anti-tumor immunity by photodynamic therapy. Immunol Res 2010; 46: 216-226.
[33] Gollnick SO, Owczarczak B and Maier P. Photodynamic therapy and anti-tumor immunity. Lasers Surg Med 2006; 38: 509-515.
[34] Panzarini E, Inguscio V and Dini L. Immunogenic cell death: can it be exploited in photodynamic therapy for cancer? BioMed Res Int 2013; 2013: 482160.
[35] Galluzzi L, Kepp O and Kroemer G. Enlightening the impact of immunogenic cell death in photodynamic cancer therapy. EMBO J 2012; 31: 1055-1057.
[36] Garg AD, Krysko DV, Vandenabeele P and Agostinis P. Hypericin-based photodynamic therapy induces surface exposure of damage-associated molecular patterns like HSP70 and calreticulin. Cancer Immunol Immunother 2012; 61: 215-221.
[37] Li W, Yang J, Luo L, Jiang M, Qin B, Yin H, Zhu C, Yuan X, Zhang J, Luo Z, Du Y, Li Q, Lou Y, Qiu Y and You J. Targeting photodynamic and photothermal therapy to the endoplasmic reticulum enhances immunogenic cancer cell death. Nat Commun 2019; 10: 3349.
[38] Deng H, Zhou Z, Yang W, Lin LS, Wang S, Niu G, Song J and Chen X. Endoplasmic reticulum targeting to amplify immunogenic cell death for cancer immunotherapy. Nano Lett 2020; 20: 1928-1933.
[39] Lifshits LM, Roque Iii JA, Konda P, Monro S, Cole HD, von Dohlen D, Kim S, Deep G, Thummel RP, Cameron CG, Gujar S and McFarland SA. Near-infrared absorbing Ru(ii) complexes act as immunoprotective photodynamic therapy (PDT) agents against aggressive melanoma. Chem Sci 2020; 11: 11740-11762.
[40] Konda P, Lifshits LM, Roque JA, Cole HD, Cameron CG, McFarland SA and Gujar S. Discovery of immunogenic cell death-inducing ruthenium-based photosensitizers for anticancer photodynamic therapy. Oncoimmunology 2020; 10: 1863626.
[41] Monro S, Colón KL, Yin H, Roque J, Konda P, Gujar S, Thummel RP, Lilge L, Cameron CG and McFarland SA. Transition metal complexes and photodynamic therapy from a tumor-centered approach: challenges, opportunities, and highlights from the development of TLD1433. Chem Rev 2019; 119: 797-828.
[42] Cerrato G, Liu P, Martins I, Kepp O and Kroemer G. Quantitative determination of phagocytosis by bone marrow-derived dendritic cells via imaging flow cytometry. Methods Enzymol 2020; 632: 27-37.
[43] Juris A, Balzani V, Barigelletti F, Campagna S, Belser P and von Zelewsky A. Ru(II) polypyridine complexes: photophysics, photochemistry, eletrochemistry, and chemiluminescence. Coord Chem Rev 1988; 84: 85-277.
[44] Wei LH, Baumann H, Tracy E, Wang Y, Hutson A, Rose-John S and Henderson BW. Interleukin-6 trans signalling enhances photodynamic therapy by modulating cell cycling. Br J Cancer 2007; 97: 1513-1522.
[45] Lamberti MJ, Mentucci FM, Roselli E, Araya P, Rivarola VA, Rumie Vittar NB and Maccioni M. Photodynamic modulation of type 1 interferon pathway on melanoma cells promotes dendritic cell activation. Front Immunol 2019; 10: 2614.
[46] Gaudino SJ and Kumar P. Cross-talk between antigen presenting cells and t cells impacts intestinal homeostasis, bacterial infections, and tumorigenesis. Front Immunol 2019; 10: 360.
[47] Dhatchinamoorthy K, Colbert JD and Rock KL. Cancer immune evasion through loss of MHC class i antigen presentation. Front Immunol 2021; 12: 636568.

[48] Rodríguez ME, Cogno IS, Milla Sanabria LS, Morán YS and Rivarola VA. Heat shock proteins in the context of photodynamic therapy: autophagy, apoptosis and immunogenic cell death. Photochem Photobiol Sci 2016; 15: 1090-1102.
[49] Fucikova J, Kepp O, Kasikova L, Petroni G, Yamazaki T, Liu P, Zhao L, Spisek R, Kroemer G and Galluzzi L. Detection of immunogenic cell death and its relevance for cancer therapy. Cell Death Dis 2020; 11: 1013.
[50] Obeid M, Tesniere A, Ghiringhelli F, Fimia GM, Apetoh L, Perfettini JL, Castedo M, Mignot G, Panaretakis T, Casares N, Métivier D, Larochette N, van Endert P, Ciccosanti F, Piacentini M, Zitvogel L and Kroemer G. Calreticulin exposure dictates the immunogenicity of cancer cell death. Nat Med 2007; 13: 54-61.
[51] Garg AD, Krysko DV, Verfaillie T, Kaczmarek A, Ferreira GB, Marysael T, Rubio N, Firczuk M, Mathieu C, Roebroek AJ, Annaert W, Golab J, de Witte P, Vandenabeele P and Agostinis P. A novel pathway combining calreticulin exposure and ATP secretion in immunogenic cancer cell death. EMBO J 2012; 31: 1062-1079.
[52] Yamazaki T, Hannani D, Poirier-Colame V, Ladoire S, Locher C, Sistigu A, Prada N, Adjemian S, Catani JP, Freudenberg M, Galanos C, André F, Kroemer G and Zitvogel L. Defective immunogenic cell death of HMGB1-deficient tumors: compensatory therapy with TLR4 agonists. Cell Death Differ 2014; 21: 69-78.
[53] Ma DY and Clark EA. The role of CD40 and CD154/CD40L in dendritic cells. Semin Immunol 2009; 21: 265-272.
[54] McLellan AD, Starling GC, Williams LA, Hock BD and Hart DN. Activation of human peripheral blood dendritic cells induces the CD86 costimulatory molecule. Eur J Immunol 1995; 25: 2064-2068.
[55] Bak SP, Barnkob MS, Bai A, Higham EM, Wittrup KD and Chen J. Differential requirement for CD70 and CD80/CD86 in dendritic cell-mediated activation of tumor-tolerized CD8 T cells. J Immunol Baltim Md 1950 2012; 189: 1708-1716.
[56] Li Z, Ju X, Silveira PA, Abadir E, Hsu WH, Hart DNJ and Clark GJ. CD83: activation marker for antigen presenting cells and its therapeutic potential. Front Immunol 2019; 10: 1312.
[57] Peng Q, Qiu X, Zhang Z, Zhang S, Zhang Y, Liang Y, Guo J, Peng H, Chen M, Fu YX and Tang H. PD-L1 on dendritic cells attenuates T cell activation and regulates response to immune checkpoint blockade. Nat Commun 2020; 11: 4835.
[58] Tsushima F, Yao S, Shin T, Flies A, Flies S, Xu H, Tamada K, Pardoll DM and Chen L. Interaction between B7-H1 and PD-1 determines initiation and reversal of T-cell anergy. Blood 2007; 110: 180-185.
[59] Wang XB, Fan ZZ, Anton D, Vollenhoven AV, Ni ZH, Chen XF and Lefvert AK. CTLA4 is expressed on mature dendritic cells derived from human monocytes and influences their maturation and antigen presentation. BMC Immunol 2011; 12: 21.
[60] Chen L. Co-inhibitory molecules of the B7-CD28 family in the control of T-cell immunity. Nat Rev Immunol 2004; 4: 336-347.
[61] Patel J, Bozeman EN and Selvaraj P. Taming dendritic cells with TIM-3: another immunosuppressive strategy used by tumors. Immunotherapy 2012; 4: 1795-1798.
[62] Bronte V and Zanovello P. Regulation of immune responses by L-arginine metabolism. Nat Rev Immunol 2005; 5: 641-654.
[63] Humeau J, Lévesque S, Kroemer G and Pol JG. Gold standard assessment of immunogenic cell death in oncological mouse models. Methods Mol Biol Clifton NJ 2019; 1884: 297-315.
[64] Rubin JB, Lagas JS, Broestl L, Sponagel J, Rockwell N, Rhee G, Rosen SF, Chen S, Klein RS, Imoukhuede P and Luo J. Sex differences in cancer mechanisms. Biol Sex Differ 2020; 11: 17.
[65] Ye Y, Jing Y, Li L, Mills GB, Diao L, Liu H and Han L. Sex-associated molecular differences for cancer immunotherapy. Nat Commun 2020; 11: 1779.
[66] Massé D, Ebstein F, Bougras G, Harb J, Meflah K and Grégoire M. Increased expression of inducible HSP70 in apoptotic cells is correlated with their efficacy for antitumor vaccine therapy. Int J Cancer 2004; 111: 575-583.
[67] Garg AD, Dudek AM, Ferreira GB, Verfaillie T, Vandenabeele P, Krysko DV, Mathieu C and Agostinis P. ROS-induced autophagy in cancer cells assists in evasion from determinants of immunogenic cell death. Autophagy 2013; 9: 1292-1307.
[68] Chao MP, Jaiswal S, Weissman-Tsukamoto R, Alizadeh AA, Gentles AJ, Volkmer J, Weiskopf K, Willingham SB, Raveh T, Park CY, Majeti R and Weissman IL. Calreticulin is the dominant pro-phagocytic signal on multiple human cancers and is counterbalanced by CD47. Sci Transl Med 2010; 2: 63ra94.
[69] Schcolnik-Cabrera A, Oldak B, Juárez M, Cruz-Rivera M, Flisser A and Mendlovic F. Calreticulin in phagocytosis and cancer: opposite roles in immune response outcomes. Apoptosis 2019; 24: 245-255.
[70] Fucikova J, Kasikova L, Truxova I, Laco J, Skapa P, Ryska A and Spisek R. Relevance of the chaperone-like protein calreticulin for the biological behavior and clinical outcome of cancer. Immunol Lett 2018; 193: 25-34.

[71] Dronca RS and Dong H. A gender factor in shaping T-cell immunity to melanoma. Front Oncol 2015; 5: 8.
[72] Morgese F, Sampaolesi C, Torniai M, Conti A, Ranallo N, Giacchetti A, Serresi S, Onofri A, Burattini M, Ricotti G and Berardi R. Gender differences and outcomes in melanoma patients. Oncol Ther 2020; 8: 103-114.
[73] Bellenghi M, Puglisi R, Pontecorvi G, De Feo A, Carè A and Mattia G. Sex and gender disparities in melanoma. Cancers 2020; 12: E1819.
[74] Klein SL and Morgan R. The impact of sex and gender on immunotherapy outcomes. Biol Sex Differ 2020; 11: 24.
[75] Krysko O, Løve Aaes T, Bachert C, Vandenabeele P and Krysko DV. Many faces of DAMPs in cancer therapy. Cell Death Dis 2013; 4: e631.
[76] Hangai S, Ao T, Kimura Y, Matsuki K, Kawamura T, Negishi H, Nishio J, Kodama T, Taniguchi T and Yanai H. PGE2 induced in and released by dying cells functions as an inhibitory DAMP. Proc Natl Acad Sci U S A 2016; 113: 3844-3849.
[77] Hayashi K, Nikolos F, Lee YC, Jain A, Tsouko E, Gao H, Kasabyan A, Leung HE, Osipov A, Jung SY, Kurtova AV and Chan KS. Tipping the immunostimulatory and inhibitory DAMP balance to harness immunogenic cell death. Nat Commun 2020; 11: 6299.
[78] Brackett CM, Owczarczak B, Ramsey K, Maier PG and Gollnick SO. IL-6 potentiates tumor resistance to photodynamic therapy (PDT). Lasers Surg Med 2011; 43: 676-685.
[79] Liu P, Zhao L, Loos F, Marty C, Xie W, Martins I, Lachkar S, Qu B, Waeckel-Énée E, Plo I, Vainchenker W, Perez F, Rodriguez D, López-Otin C, van Endert P, Zitvogel L, Kepp O and Kroemer G. Immunosuppression by mutated calreticulin released from malignant cells. Mol Cell 2020; 77: 748-760, e9.
[80] Roh JS and Sohn DH. Damage-associated molecular patterns in inflammatory diseases. Immune Netw 2018; 18: E27.
[81] Hernandez C, Huebener P and Schwabe RF. Damage-associated molecular patterns in cancer: a double-edged sword. Oncogene 2016; 35: 5931-5941.
[82] Oh SA, Wu DC, Cheung J, Navarro A, Xiong H, Cubas R, Totpal K, Chiu H, Wu Y, Comps-Agrar L, Leader AM, Merad M, Roose-Germa M, Warming S, Yan M, Kim JM, Rutz S and Mellman I. PD-L1 expression by dendritic cells is a key regulator of T-cell immunity in cancer. Nat Cancer 2020; 1: 681-691.
[83] Brunner-Weinzierl MC and Rudd CE. CTLA-4 and PD-1 control of T-cell motility and migration: implications for tumor immunotherapy. Front Immunol 2018; 9: 2737.
[84] Hsu FJ and Komarovskaya M. CTLA4 blockade maximizes antitumor T-cell activation by dendritic cells presenting idiotype protein or opsonized anti-CD20 antibody-coated lymphoma cells. J Immunother Hagerstown Md 1997 2002; 25: 455-468.
[85] Laurent S, Carrega P, Saverino D, Piccioli P, Camoriano M, Morabito A, Dozin B, Fontana V, Simone R, Mortara L, Mingari MC, Ferlazzo G and Pistillo MP. CTLA-4 is expressed by human monocyte-derived dendritic cells and regulates their functions. Hum Immunol 2010; 71: 934-941.
[86] Mayoux M, Roller A, Pulko V, Sammicheli S, Chen S, Sum E, Jost C, Fransen MF, Buser RB, Kowanetz M, Rommel K, Matos I, Colombetti S, Belousov A, Karanikas V, Ossendorp F, Hegde PS, Chen DS, Umana P, Perro M, Klein C and Xu W. Dendritic cells dictate responses to PD-L1 blockade cancer immunotherapy. Sci Transl Med 2020; 12: eaav7431.